

# Constraints on the strength of faults from the geometry of rider blocks in continental and oceanic core complexes

Eunseo Choi<sup>1,2</sup> and W. Roger Buck<sup>1</sup>

Received 3 August 2011; revised 29 February 2012; accepted 6 March 2012; published 28 April 2012.

[1] Large offset normal faults, central to the formation of core complexes, require a minimum amount of fault weakening to form according to analytic and numerical models. New work suggests that these faults cannot be too weak and still result in the kind of fault-bounded rider blocks overlying the lower plate of some large offset normal faults. Rider block wedges of upper plate rocks, including syn-tectonic sedimentary rocks, are often seen on continental metamorphic core complexes. Blocks of volcanic rocks are sometimes seen to bury the detachment of oceanic core complexes. We consider extensional faulting in Mohr-Coulomb layers to estimate the conditions that can lead to rider block formation and estimate the size of rider blocks formed. Offset of a single normal fault causes rotation of the fault, with the shallow part of the fault rotating more than the deeper parts. In models, rider blocks form when the shallow section of a normal fault becomes rotated so far from an optimal dip that it is replaced by a new, steeper-dipping splay fault that links with the deeper part of the old fault. Analytic theory predicts a narrow range of fault weakening that leads to large offset normal faults with rider blocks. Infill of sediments or volcanics into the basin formed by offset of a single normal fault also promotes rider block development. For a 10 km-thick brittle layer complete cohesion losses greater than 15 MPa are too large to result in rider-block formation. Significant reduction in fault friction can prevent rider block formation. With sufficient infill the rider blocks up to nearly 10 km<sup>2</sup> in cross-sectional area, similar to those observed, can result. Numerical models confirm the general predictions of the analytic model, but also show that precise relations between block size and amount of fault weakening must await higher resolution models.

**Citation:** Choi, E., and W. R. Buck (2012), Constraints on the strength of faults from the geometry of rider blocks in continental and oceanic core complexes, *J. Geophys. Res.*, 117, B04410, doi:10.1029/2011JB008741.

## 1. Introduction

[2] One of the most important and contentious issues in geodynamics concerns the weakness of faults. Faults must be weaker than their surroundings so that strain will concentrate on them but observations have not firmly established how weak faults are. Fault strength is often described in terms of a friction coefficient and there is debate over the level of friction. The ‘strong fault’ view is that faults have friction coefficients between 0.6 and 0.8, like those measured in the laboratory for most rocks [Byerlee, 1978]. Stress differences measured in boreholes around the world are usually close to the level required for slip on faults with such normal levels of friction [e.g., McGarr and Gay, 1978; Brace and Kohlstedt, 1980; Townend and Zoback, 2000] and this supports the ‘strong’ view.

[3] The ‘weak fault’ view is that faults have much lower coefficients of friction than 0.6. The orientation of stresses close to the San Andreas fault [e.g., Mount and Suppe, 1987; Zoback and Healy, 1992] and the lack of a localized heat flow anomaly over the San Andreas [Lachenbruch and Sass, 1992] argue for weak faults. The recognition of large-offset normal faults, or detachments, in metamorphic core complexes [e.g., Coney, 1980] that presently dip at a low angle, or are flat, have also been used as an argument that these faults are weak [e.g., Wernicke, 1981; Davis and Lister, 1988].

[4] The association of continental metamorphic core complexes with large offset of a major normal fault [e.g., Coney, 1980; Davis, 1980; Davis et al., 1983] was a surprising discovery in structural geology. It prompted an energetic debate over whether detachments formed at lower dip angles than suggested by simple rock mechanics [e.g., Wernicke, 1981; Spencer, 1984; Davis et al., 1986], or whether inactive parts of the fault rotated to a low angle [e.g., Buck, 1988; Wernicke and Axen, 1988]. Formation of normal faults with dips lower than 30° would require that the fault be much weaker than the surrounding rocks. Though there is evidence for some rotation of detachments to lower dips, some authors claim

<sup>1</sup>Lamont-Doherty Earth Observatory, Earth Institute at Columbia University, Palisades, New York, USA.

<sup>2</sup>Now at Institute for Geophysics, University of Texas, Austin, Texas, USA.

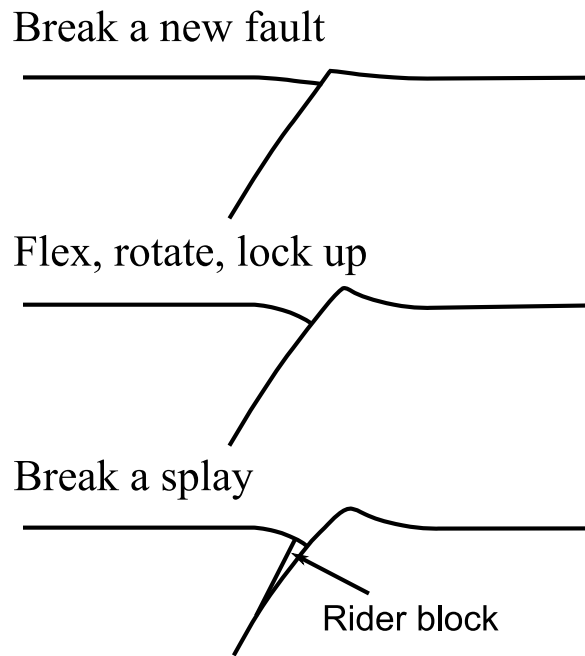


**Figure 1.** Schematic diagram that depicts the process of rider block formation. (top) A newly formed normal fault with small offset in a brittle layer. (middle) The brittle layers flexes and the fault rotates eventually locking up as offset increases. (bottom) When the existing fault locks up, a splay fault forms to continue to accommodate extension.

that some continental detachments initiate with dips less than  $30^\circ$  [e.g., Davis and Lister, 1988; Scott and Lister, 1992]. The question of the dip angle for formation of oceanic detachments has been firmly resolved in favor of high-angle initiation based on the large magnitude of rotation indicated by paleo-magnetic analysis of cores drilled in the Atlantis Massif OCC [Morris et al., 2009].

[5] Rider blocks or rafted blocks are conceptualized in this study as pieces of hanging wall rocks that get cut off and transferred to the footwall side of the active portion of the detachment system (Figure 1). They are seen on both continental (Figure 2) and oceanic detachments (Figure 3) [e.g., Davis, 1980; Reston and Ranero, 2011]. Rider blocks are thought to form when a normal fault is rotated to such a low dip that it locks up and a new fault forms (Figure 1) [e.g., Buck, 1988; Smith et al., 2008; Schouten et al., 2010; Reston and Ranero, 2011]. The amount of rotation before a fault locks up depends on the strength of the fault compared to the strength of the rock it cuts [e.g., Sibson, 1985; Nur et al., 1986; Scholz et al., 2010]. Thus, constraining where rider blocks form and how rotated a fault is when they form can constrain the weakness of faults.

[6] In this paper we use basic rock mechanics theory and numerical experiments on fault development to quantify the relation between fault strength, the level of basin infill and rider block formation. We treat fault weakening both in terms of reduction in cohesion and/or friction coefficient. Our results allow us to quantify recent predictions of Reston and Ranero [2011] regarding oceanic core complexes, but the results also should apply to continental core complexes.

Most importantly, we show that the geometry of rider blocks constrains the range of detachment fault strength.

## 2. Observations and Interpretations of Core Complexes and Rider Blocks

[7] The key role played by large offset normal faults, or extensional detachments, in the formation of continental metamorphic core complexes (MCCs) was discovered in the late 1970s [e.g., Coney, 1980]. The fact that such detachments typically dip at a very low angles, or are essentially horizontal, led to the idea that our fundamental understanding of rock mechanics might be flawed. Many ideas were advanced to explain faults slipping with low dip angles. By analogy with the problem of low-angle thrusts [Hubbert and Rubey, 1959], some authors claimed that pore pressures could be elevated on some special normal faults [Axen, 1992]. The question of initiation of normal faults with low-dips prompted development of models of special conditions that would produce highly rotated stress fields [e.g., Yin, 1989]. However, careful analysis of the fault failure indicates that faults tend not to form in regions of rotated stresses [e.g., Wills and Buck, 1997].

[8] Seismic constraints on the dips of active, seismogenic normal faults show that most have dips between  $\sim 45^\circ$  and  $60^\circ$  [e.g., Jackson, 1987]. The extreme extension implied by large offset normal faults should produce considerable crustal thinning and subsidence. Several authors note that flow of lower crust into the region of upper crustal extension may explain why core complexes are not seen as topographic lows [e.g., Block and Royden, 1990; Kruse et al., 1991; Buck, 1991]. Some authors claim that magma intrusion [Gans et al., 1985] or diapirs of subducted material may be needed [Martinez et al., 2001; Ellis et al., 2011].

[9] Oceanic detachment faults were recognized on slow spreading ridges in the last 15 years [Cann et al., 1997] mainly from mapping of low-dip-angle corrugated fault surfaces, which are sometimes described as mega-mullions [e.g., Tucholke et al., 1998]. The footwalls of oceanic detachments typically include gabbros and/or peridotites [Escartin et al., 1997] and the system that includes related structures is termed an oceanic core complex, or OCC [e.g., Cann et al., 1997].

[10] Figure 3 shows a map view of an OCC along with a block diagram showing the possible geometry of rider blocks. Rider blocks are seen only on parts of some continental and oceanic core complexes. Erosion could have plausibly removed rider blocks from continental core complexes but the lack of submarine erosion simplifies interpretation of the distribution of oceanic rider blocks.

[11] Reston and Ranero [2011] surveyed data on rider blocks and suggested that whether or not rider blocks form on oceanic core complexes depends on 2 factors: the strength of a detachment fault and the level of volcanic infill of the basin above an active detachment. They noted that the strength of an oceanic detachment may depend on the composition of the faults rocks. Specifically, the alteration of ultramafic rocks can produce rocks like serpentinite and talc with extremely low coefficients of friction. In contrast basalt and gabbro fault rocks may be little altered and could maintain larger friction coefficients. Thus, they suggested that oceanic rider blocks should form only where basalt or

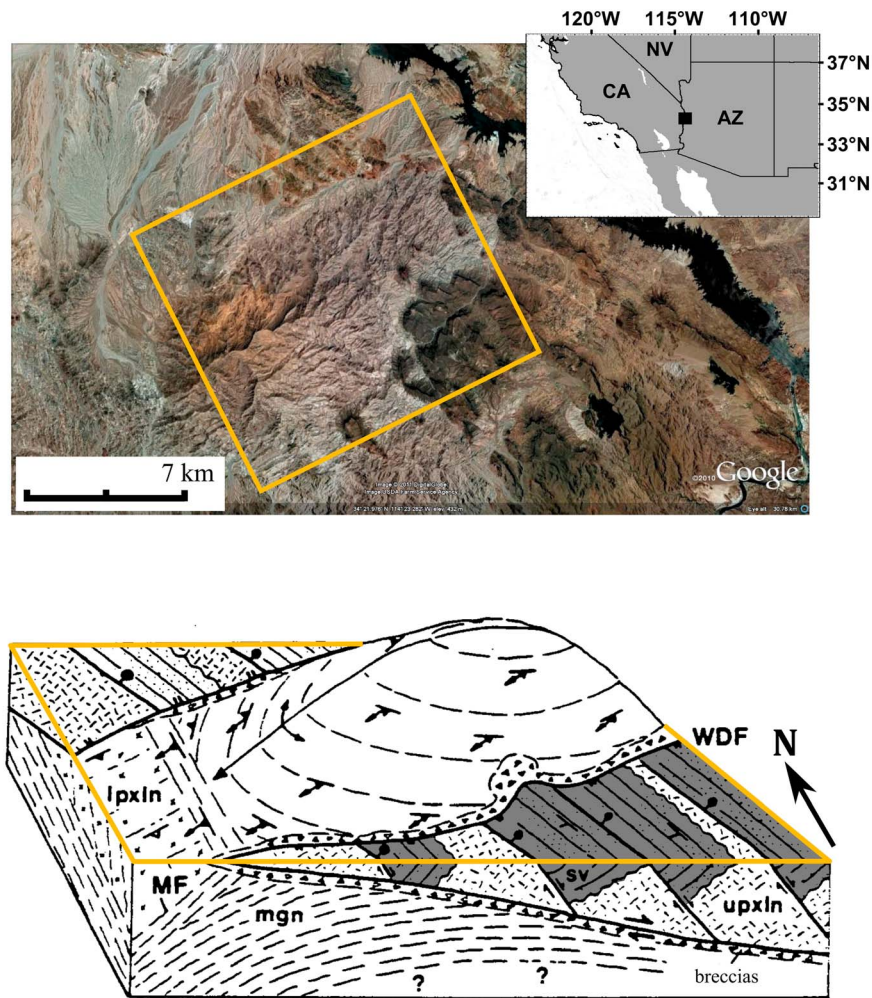


**Figure 2.** (top) Satellite image of Whipple Mountains in the southeastern California (Copyright Google Inc., used with permission; 2011 DigitalGlobe). The yellow-lined box approximately marks the location of the schematic diagram. Black solid square in the inset provides the geographic reference for the image. CA, NV, and AZ in the inset denote California, Nevada, and Arizona state, respectively. (bottom) A schematic block diagram showing geologic structures in the region, including rider blocks [after Davis, 1988]. Topography is not in scale. The gray-shaded units to the south correspond to the distinctively dark rocks in the satellite image, which constitutes the current surface of rider blocks. Abbreviations: MF = mylonitic front; WDF = Whipple Mountains Detachment Fault; cbr = chloritic breccias; lpxln = lower plate crystalline rocks; mgn = mylonitized gneiss; sv = sedimentary and volcanic rocks; upxln = upper plate crystalline rocks.

gabbro is a major rock type and where there is extrusive infill. To test this hypothesis and to define the general conditions for rider block formation we begin with a classical treatment of the conditions for fault slip.

### 3. Limits on Fault Rotation

[12] According to Mohr-Coulomb theory, a fault should form with an orientation (relative to principal stress axes) that minimizes the stress difference needed for fault slip. Assuming that principal stress axes are either parallel or orthogonal to the earth's surface allowed Anderson [1942] to show that normal faults should form with dips greater than  $45^\circ$ . For a typical friction coefficient  $f = 0.6$ , a normal

fault should form with a dip of about  $60^\circ$ . Intact rocks are cohesive and therefore cohesion, the maximum shear stress that rock can sustain even when normal stress is zero, is the other important parameter in Mohr-Coulomb theory. Faults may evolve to be weaker than surrounding rocks because the fault cohesion ( $C$ ) and/or friction coefficient is reduced although cohesion does not affect their orientation unlike friction coefficient. Weak faults can continue to slip even if they rotate away from their ideal orientation. Nur *et al.* [1986] used Mohr-Coulomb theory to calculate how far faults can rotate before they should be replaced by a new, optimally oriented fault. Here, we apply the Nur *et al.* [1986] approach to the formation of rider blocks under particular

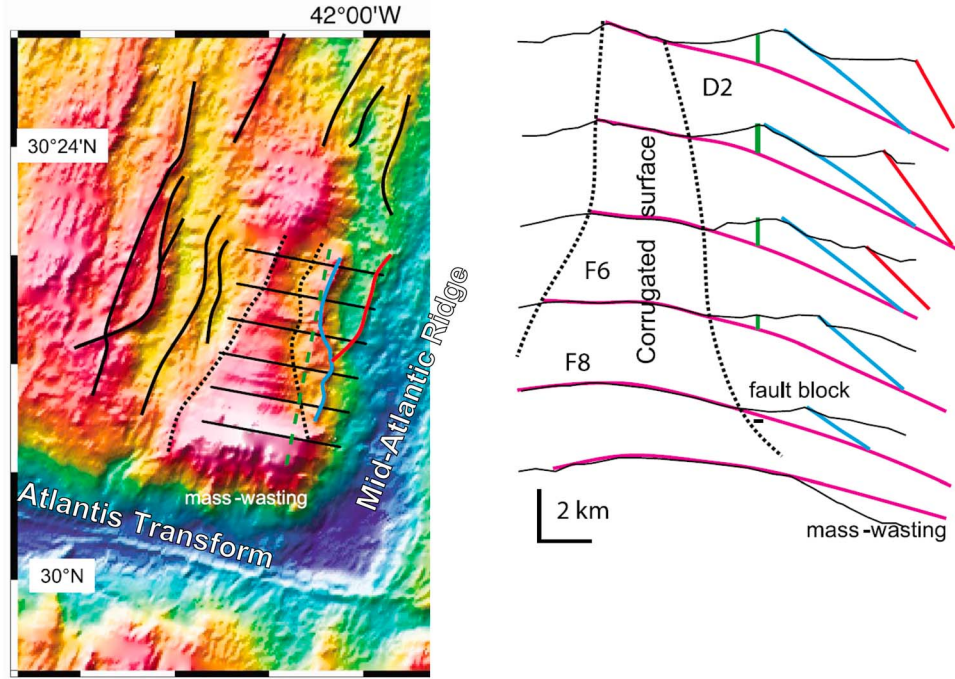


**Figure 3.** (left) Bathymetry of the North Atlantis Inside Corner, showing the corrugated surface of the Atlantis Massif narrowing to the north as increasing numbers of fault blocks develop between the exhumed slip surface and the spreading axis. (right) Bathymetric profiles across this structure, showing interpretation in which the slip surface continues beneath these fault blocks to the north: the fault blocks represent successive slices of the hanging wall (blue then black then red) sliced off the hanging wall in a rolling hinge model. The location of the detachment is constrained by seismic profile Meg-5 [Canales *et al.*, 2004]: green line on map and green bars on profiles showing depth to “detachment” [Reston and Ranero, 2011].

assumptions about the geometric development of large-offset normal faults.

[13] For a quantitative analysis, we start from the assumption that the maximum and minimum effective compressive principal stresses,  $\sigma'_1$  and  $\sigma'_3$ , are identified with vertical ( $\sigma'_{yy}$ ) and horizontal ( $\sigma'_{xx}$ ) stresses, respectively and given by

$$\begin{aligned}\sigma'_1 &= \sigma'_{yy} = \rho gy - P_f \\ \sigma'_3 &= \sigma'_{xx} = \rho gy - P_f + \Delta\sigma_{xx},\end{aligned}\quad (1)$$

where  $\rho$  is the density,  $g$  is the gravitational acceleration,  $y$  is the vertical coordinate (positive downward),  $P_f$  is pore fluid pressure, and  $\Delta\sigma_{xx}$  is the horizontal differential stress and tensional. Normal and shear stresses on a plane at an angle  $\theta$  with  $y$  axis are given by [e.g., Turcotte and Schubert, 2002]

$$\begin{aligned}\sigma_n &= \frac{1}{2}(\sigma'_{xx} + \sigma'_{yy}) + \frac{1}{2}(\sigma'_{xx} - \sigma'_{yy})\cos 2\theta, \\ \tau &= -\frac{1}{2}(\sigma'_{xx} - \sigma'_{yy})\sin 2\theta.\end{aligned}\quad (2)$$

By substituting (1) into (2), we get

$$\begin{aligned}\sigma_n &= (\rho gy - P_f) + \frac{\Delta\sigma_{xx}}{2}(1 + \cos 2\theta), \\ \tau &= -\frac{\Delta\sigma_{xx}}{2}\sin 2\theta.\end{aligned}\quad (3)$$

At failure, the shear and normal stress components are related by the Mohr-Coulomb failure criterion,  $\tau = f\sigma_n + C$ , where  $f$  is the coefficient of internal friction and  $C$  is cohesion. Thus, we get the following expression for differential stress as a function of depth and failure parameters:

$$|\Delta\sigma_{xx}| = \frac{2f(\rho gy - P_f) + 2C}{\sin 2\theta + f(1 + \cos 2\theta)}.\quad (4)$$

The absolute value of  $\Delta\sigma_{xx}$  for initial values of frictional parameters ( $f_i$  and  $C_i$ ), an effective lithostatic pressure ( $\rho gy - P_f$ ), and the initially optimal fault orientation ( $\theta_i$ ) is denoted as  $\Delta\sigma'_{xx}$  and acquired from the equation (4). If we consider hydrostatic pore pressures, then the equations derived here hold with an effective rock density:  $\rho = \rho_c - \rho_w$ , where  $\rho_c$  and  $\rho_w$  are crust and fluid density, respectively. The value of effective density is always fixed to be  $1800 \text{ kg/m}^3$  ( $\rho_c$  and  $\rho_w$  are  $2800$  and  $1000 \text{ kg/m}^3$ , respectively) in this study. This way, we can drop the pore fluid pressure term in the equations hereafter. Since  $\theta_i$  is related to  $f_i$  as well as to the initial friction angle ( $\phi_i$ ) by  $\tan 2\theta_i = 1/f_i = 1/\tan \phi_i$ :

$$\Delta\sigma'_{xx} = \frac{2f_i \rho gy + 2C_i}{\sqrt{1 + f_i^2} + f_i}.\quad (5)$$

We now evaluate how much the dip of a fault can be reduced from the initial optimal angle when the fault



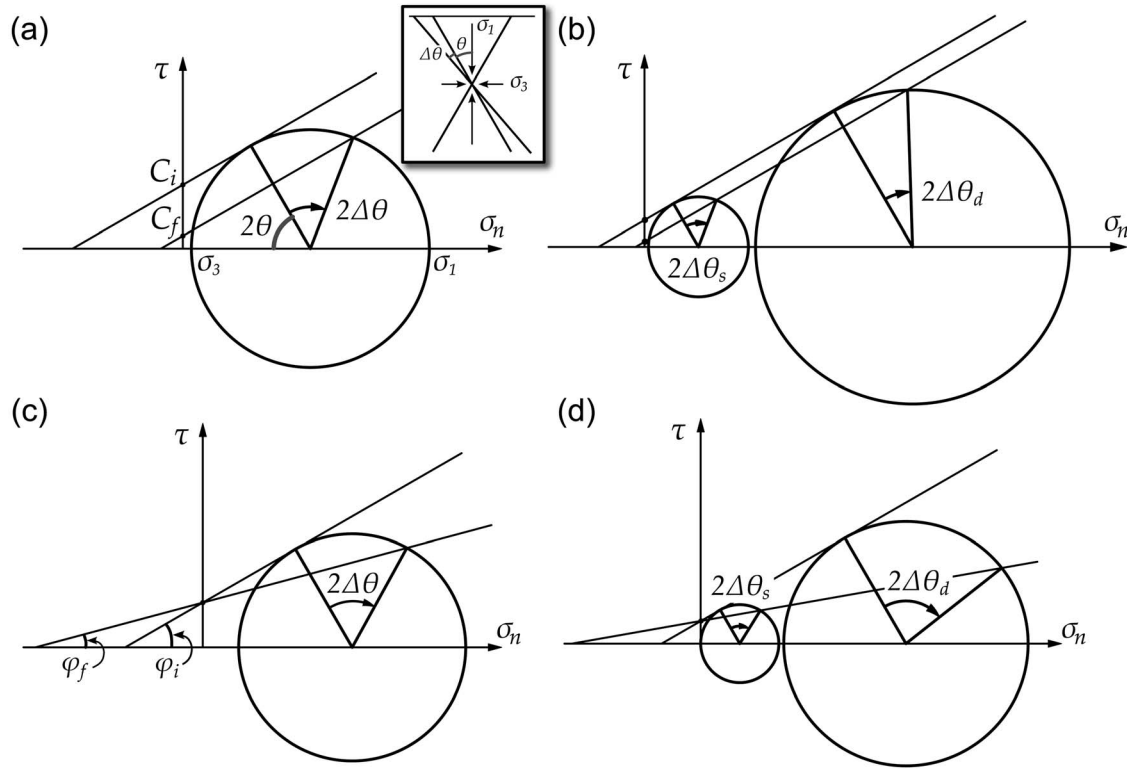


**Figure 4.** Diagram showing how Mohr circles are intersected by Mohr-Coulomb failure envelopes for cohesion reduction and friction reduction. An optimally oriented existing fault is allowed to rotate by  $\Delta\theta$  without locking. (a) The initial cohesion  $C_i$  is reduced to  $C_f$  while friction angle remains unchanged.  $\sigma_1$  and  $\sigma_3$  are the greatest and the least compressional principal stresses. The inset shows the geometric relations between the principal stresses and fault orientations. (b) Two failure envelopes for  $C_i$  and  $C_f$  as well as two Mohr circles corresponding to two different depths. The maximum rotation for the shallow circle is denoted as  $\Delta\theta_s$ ;  $\Delta\theta_d$  for the deep one. (c) The initial friction angle  $\phi_i$  is reduced to  $\phi_f$  while a non-zero cohesion remains unchanged. (d) Same as Figure 4b except that the failure envelopes have different friction angles.

becomes weaker. The weaker fault is characterized by final values of the friction coefficient  $f_f$  and the cohesion  $C_f$ . The maximum allowable fault rotation  $\Delta\theta = \theta_{\max} - \theta_i$ .  $\theta_{\max}$  is the maximum of all  $\theta$  for which  $|\Delta\sigma_{xx}| \leq \Delta\sigma'_{xx}$  and acquired by solving the following transcendental equation for  $\theta$ :

$$\frac{2f_f \rho g y + 2C_f}{\sin 2\theta + f_f(1 + \cos 2\theta)} = \frac{2f_i \rho g y + 2C_i}{\sqrt{1 + f_i^2} + f_i}. \quad (6)$$

The maximum allowable fault rotation  $\Delta\theta$  becomes independent of depth ( $y$ ) when cohesion is zero or  $f_f/f_i = C_f/C_i$ . In practice, closed form solutions can be acquired using the geometry of Mohr circles and failure envelopes [e.g., Nur *et al.*, 1986]. See Appendix A for the complete solutions.

[14] On a Mohr circle diagram, cohesion reduction is equivalent to a down-shift of a failure envelope. If a Mohr circle was tangential to a failure envelope for an initial cohesion, the shifted envelope due to reduced cohesion now intersects the circle, defining the angle  $\Delta\theta$ , the maximum angle of rotation (Figure 4a). The value of  $\Delta\theta$  depends not only on the amount of cohesion reduction but also on the depth. When another Mohr circle for a larger confining

pressure at a greater depth is drawn next to a shallower-depth counterpart, we can see that fault rotation is more limited at the greater depth for given cohesion reduction (Figure 4b). A slope change due to friction angle reduction will also result in the intersection of the failure envelope and the Mohr circle (Figure 4c). The range of allowable orientations for active faults is not symmetric about  $\theta_i$ , as it is for a reduction in cohesion only. Also, the depth-dependence is reversed compared to the case of cohesion reduction in that a larger amount of rotation is possible at greater depths (Figure 4d).

[15] Plots of  $\Delta\theta$  with depth, which we term “rotation envelopes,” are made by substituting into equation (6) a series of values of initial friction angle and cohesion ( $\phi_i$  and  $C_i$ ) as well as their reduced final values ( $\phi_f$  and  $C_f$ ). We show several rotation envelopes for  $C_i$  of 3 and 30 MPa and  $\phi_i$  of  $30^\circ$  (Figure 5). A fault is allowed to rotate more at shallower depths if the fault is weakened by cohesion reduction only (Figure 5a). A fault with cohesion reduced to zero can continue to slip even if it becomes almost flat ( $0^\circ$  dip) near surface. The same trend holds for a larger initial cohesion of 30 MPa but the overall magnitude of allowable rotation is much larger (Figure 5b). The opposite (i.e., downward-widening) trend between  $\Delta\theta$  and depth is seen when the

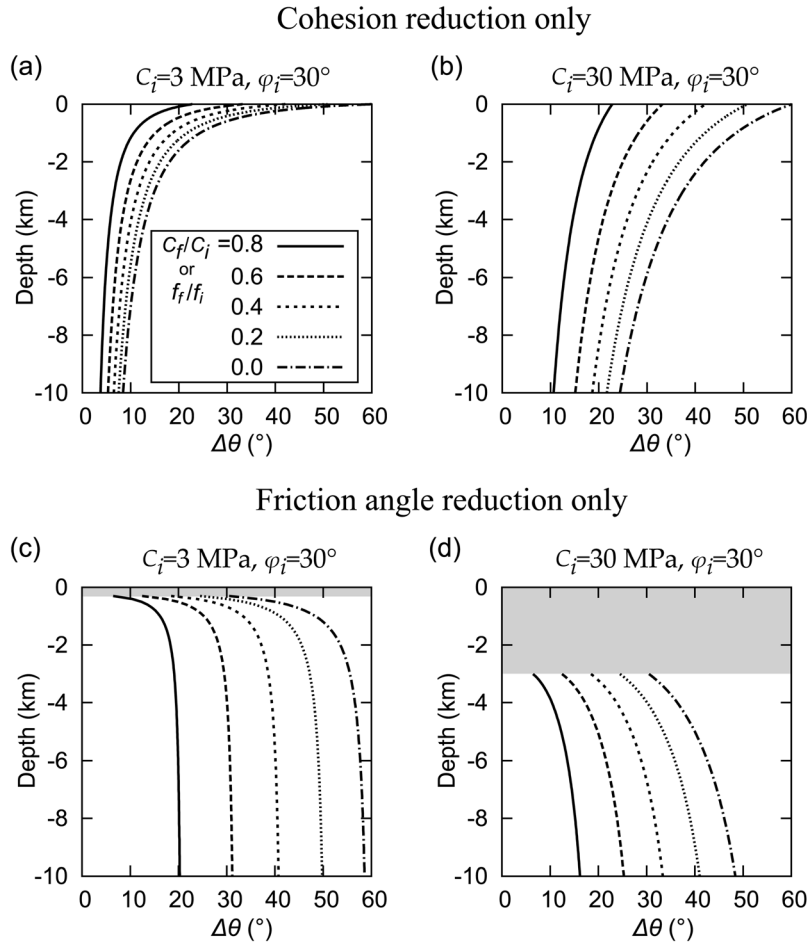


**Figure 5.** Rotation envelopes, i.e.,  $\Delta\theta$ -depth plots, for (a, b) cohesion reduction only and (c, d) friction angle reduction only. The initial value of cohesion ( $C_i$ ) is 3 MPa in Figures 5a and 5c and 30 MPa in Figures 5b and 5d.  $\varphi_i$  is  $30^\circ$  for all plots. The gray areas in Figures 5c and 5d represent the depth range in which failure is prevented by friction angle reduction. See the text for details.

fault weakening occurs by friction angle reduction only (Figures 5c and 5d for  $C_i = 3$  and 30 MPa, respectively). This trend was also found by Axen [2004]. When the initial cohesion is lower, the rotation envelopes are shifted toward greater  $\Delta\theta$ . Where confining pressure is sufficiently low and tension failure is expected,  $\Delta\theta$  for friction angle reduction is not defined (gray region in Figures 5c and 5d).

[16] The same exercise can be repeated for a more general situation where cohesion and friction angle are reduced simultaneously (Figure 6). When cohesion and the friction angle are reduced by the same proportion, the dependence on depth as well as  $C_i$  disappears (Figure 6a). If reduced by different proportions, the trend corresponding to the most reduced parameter becomes dominant. For instance, if  $\varphi_f/\varphi_i$  is set to be  $0.5(C_f/C_i)$ , the friction angle is reduced by 75% while cohesion is reduced by 50%. In this case, the widening-downward trend seen in the cases of friction reduction reappears (Figure 6b).

#### 4. Rotation of Normal Faults With Offset

[17] To use the rotation envelopes to estimate when rider blocks form we need to know about how a fault rotates with

offset. The offset of a normal fault causes an isostatic response that can rotate the fault [Vening-Meinesz, 1950; Buck, 1988]. Low-angle normal faults are considered to have experienced large amounts of rotation and offset although they were originally created with a higher dip. The deviation from the original dip grows larger as the fault offset is increased. If the fault becomes sufficiently weak during this process, the low-angle fault can remain active; otherwise, it would eventually stop slipping and a new fault should be created to accommodate further extension.

[18] We want to quantify this flexural fault rotation as a function of depth. To do this, we use numerical models where faults are taken to be zones of localized plastic strain following the approach of Poliakov and Buck [1998] (Figure 7). The model domain represents a block of brittle lithosphere that is 100 km wide and 10 km thick. The model resolution is 500 m. Lamé constants are 30 GPa, density is  $2700 \text{ kg/m}^3$ , the initial friction angle ( $\varphi_i$ ) is  $30^\circ$  and the initial cohesion ( $C_i$ ) is 30 MPa. Dilation angle is set to be  $0^\circ$ . The full extension rate is 2 cm/yr. Only cohesion is reduced from the initial value to 3 MPa as a linear function of plastic strains between 0 and 0.9. The brittle layer is assumed to overlie an inviscid substrate and has a free top surface. The

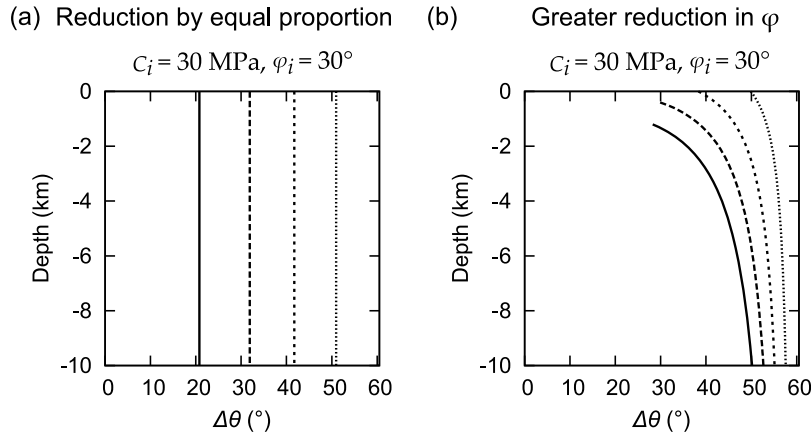


**Figure 6.** As in Figure 5 but cohesion and friction angle are reduced simultaneously: (a) reduced by equal proportions; (b) friction angle is reduced more than cohesion such that  $\phi_f/\phi_i = 0.5(C_f/C_i)$ . For legends, see Figure 5.

brittle-ductile boundary is assumed to remain flat following *Lavier et al.* [2000]. One model leaves the depression over the active fault empty while the second model simulates filling the depression with sediment. We follow *Bialas and Buck* [2009] for the numerical treatment of sedimentary infill. The sedimentary infill is taken to have the same elastic and Coulomb properties as the original lithosphere but less dense by  $500 \text{ kg/m}^3$ .

[19] Locations of the maximum plastic strain, taken to mark the position of the fault, are plotted for different time steps, 0.1, 0.3, 0.5, 1.5 and 2.5 My (Figure 7a, dotted lines). We then fit these discrete fault profiles to spline curves (Figure 7a, solid lines). This step is necessary because dip angle at a location on the faults is equivalent to local slope, a derivative quantity that is sensitive to the smoothness of the profiles. Finally, the smoothed fault profiles are mapped in  $\Delta\theta$ -depth space, where  $\Delta\theta$  is measured with respect to the optimal orientation for  $\phi_0 = 30^\circ$  (Figure 7b). The profiles of finite-offset normal faults in numerical models appear as nearly straight lines in the  $\Delta\theta$ -depth space. The lower parts of the faults have dips equal to or slightly higher than the optimal one due to flexural rotation and are cut off from the plot (Figure 7b). After offset of about twice the layer thickness, fault profiles in both models converged to a steady state geometry. They also show, more clearly in the model with infill, that the fault has rotated maintaining a curved shape.

## 5. Predicting Fault Locking Depths From Rotation Envelopes

[20] We expect rider blocks to form only if rotated faults are not too weak. Ideally, we would do a series of numerical models of fault offset and rotation with different fault weakening parameters to see when rider blocks form. Unfortunately, this requires extremely high numerical resolution and so the time to run many cases is prohibitive. Thus, we here report results from high resolution models that were started with the kind of curved faults appearing linear in  $\Delta\theta$ -depth space like those seen in the lower resolution models of the previous section.

[21] Here we use the curved geometry of a rotated normal fault to examine conditions that lead to the emergence of a

rider block. Using numerical models, we verify the above analysis on the fault stability, i.e., the locking conditions for a given fault geometry, rather than attempt to simulate the process of fault rotation.

[22] The model domain is a 5 km-thick and 20 km-wide extending crustal block. We assume a curved normal fault that is linear in  $\Delta\theta$ -depth space (Figure 8a). The condition that the slope angle is a linear function of depth implies that the geometry of the fault profile should take a form of  $z' \sim \sin^{-1}(\exp(-x'))$ , where  $x'$  and  $z'$  are properly scaled horizontal and vertical coordinates (see Appendix B for details). In the examples shown in Figure 8, the fault dip is  $60^\circ$  at the bottom and  $10^\circ$  at the top. The fault has a reduced cohesion compared to the surrounding material while all the other material properties are uniform. Elastic material properties, the initial plastic parameters, and boundary conditions are the same as those in the previous section but the model resolution is  $\sim 50 \text{ m}$ . The effective rock density is  $1800 \text{ kg/m}^3$  and the rotation envelopes are calculated for this density. The calculation was run for only a small amount of deformation so that the stress orientations remain close to those assumed in the analytical calculations: i.e.,  $\sigma_1$  and  $\sigma_3$  are vertical and horizontal, respectively. The numerical solution was acquired using the code SNAC [*Choi et al.*, 2008].

[23] The results confirm that not only does a fault lock where the rotation limit is exceeded but also a new fault branch is created forming a rider block. The case of reduced cohesion ( $C_f$ ) equal to 3 MPa (i.e.,  $C_f/C_i = 0.1$ ) is shown in Figure 8a. Since the fault orientation is within the rotation limit at all depths, the entire fault remains active without locking. When the cohesion is reduced less ( $C_f/C_i = 0.5$ ), the near-surface portion of the fault exceeds rotation limits at depths  $< 2.5 \text{ km}$  and locks. A new fault branch is then created rooted at the depth where the fault profile intersects the rotation envelope (Figure 8b).

## 6. Formation Condition and Size of Rider Blocks

[24] We are encouraged that a numerical model can produce a splay fault defining a potential rider block. However, numerically mapping out the range of conditions leading to rider block formation would take a very long

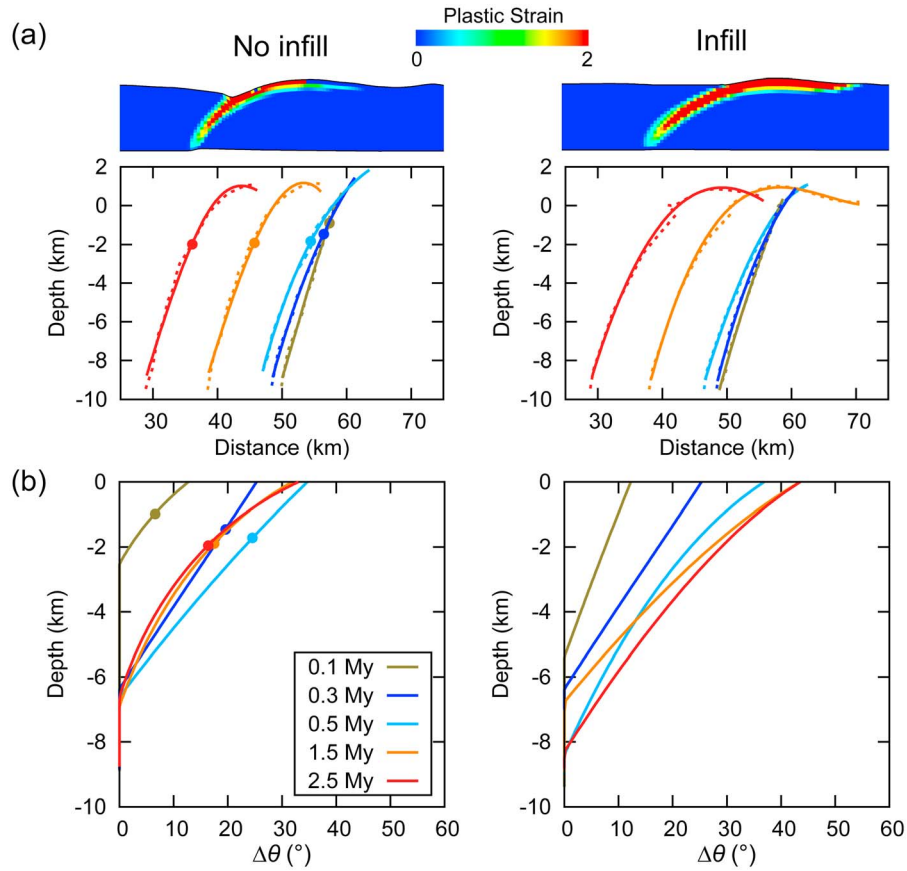


**Figure 7.** The evolution of fault geometry without sedimentary infill (left) and with infill up to zero level (right). (a) (top) Plastic strain distribution after 1.5 My of model time representing rotated faults. (bottom) Fault profiles at different model times constructed by first connecting the locations of maximum plastic strain per depth (dotted lines) and then fitting them with spline curves (solid lines). Solid circles on each profile of no-infill cases indicate the depth at which the fault is exposed on the surface. (b) Fault profiles mapped on the  $\Delta\theta$ -depth space.

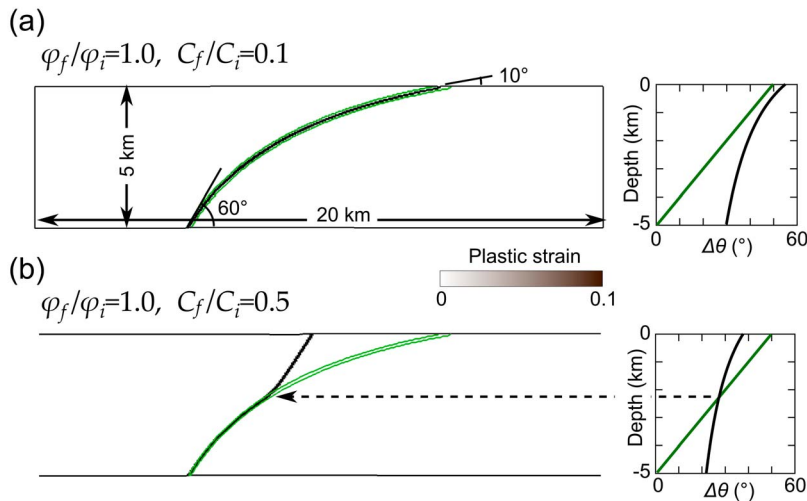


**Figure 8.** Stability of modeled accurate faults as a function of cohesion reduction. (a) (left) The second invariant of plastic strain is shown in gray color scale and the original fault geometry with green lines. (right) The original fault geometry mapped to the  $\Delta\theta$ -depth space (green) and a rotation envelope for  $C_f/C_i = 0.1$  (black). (b) Same as Figure 8a but  $C_f/C_i = 0.5$ . Dashed lines connect the predicted locking depth and the modeled. The effective rock density is  $1800 \text{ kg/m}^3$ ,  $\varphi_i = 30^\circ$  and  $C_i = 30 \text{ MPa}$  for both cases.



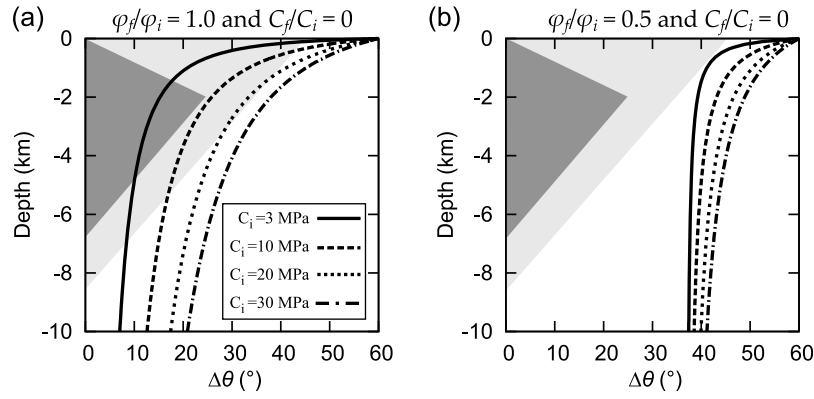


**Figure 9.**  $\Delta\theta$ -depth plots for the cases with (a)  $\phi_f/\phi_i = 1.0$  or (b) 0.5. The value of  $C_i$  has a range of 3 to 30 MPa but  $C_f/C_i = 0$  for all the cases. Dark gray area represents the region in the  $\Delta\theta$ -depth space swept by fault profiles from the no-infill case in Figure 8; light gray area for the with-infill case.

time. Fortunately, it is possible to analytically predict conditions for rider block formation using rotation envelopes, as defined here, combined with the assumption on the fault geometry that the fault's slope linearly changes with depth.

[25] Based on our numerical models of normal fault development, we assume that the overall curvature of the fault increases with increasing offset, gradually approaching the limiting geometry with the shallowest surface dip angle. The continuous change in curved fault geometry by progressive fault offset would sweep out a triangular region on a  $\Delta\theta$ -depth plot as shown in Figure 9. Such a region on a  $\Delta\theta$ -depth plot is bounded by the limiting geometry and the infill level (or the depth where a fault is exposed on the surface in case of no infill). We term such a region a “fault profile domain” and plot those for the two models in Figure 9: dark gray for the no-infill case and light gray for the infill one.

[26] For the cases illustrated, both fault profile domains overlap with some rotation envelopes corresponding to several values of  $C_i$  with  $C_f/C_i = 0.0$  and  $\phi_f/\phi_i = 1.0$

(Figure 9a). In this weakening scenario and after sufficient amount of rotation, faults would lock and thus a rider block would form depending on their  $C_i$  values. The fault profile domain of the no-infill case overlaps with the envelopes with  $C_i \leq 10$  MPa while that of the with-infill case does with higher  $C_i$  envelopes. When the friction angle is also reduced ( $\phi_f/\phi_i = 0.5$ ), neither region overlaps with the rotation envelopes (Figure 9b) suggesting that rider blocks are harder to form if a fault is weakened by both cohesion and friction angle reduction.

[27] We assume that a splay fault forms when the force to cut such a new fault segment is equal to or less than that required for the continued slip on the older, rotated fault. The new fault splay is taken to form with the ideal dip angle and to reach from the surface to a depth of intersection with the original fault. To compute the intersection depth, we integrate the differential stress for slip ( $\Delta\sigma_{xx}$ ) from the surface to depth  $z$  which gives us the force  $F_s(z)$  for slip on that section of faults.  $F_s$  as a function of depth is computed for both the rotated fault, with reduced cohesion and/or friction, and the potential splay, with the initial values of cohesion

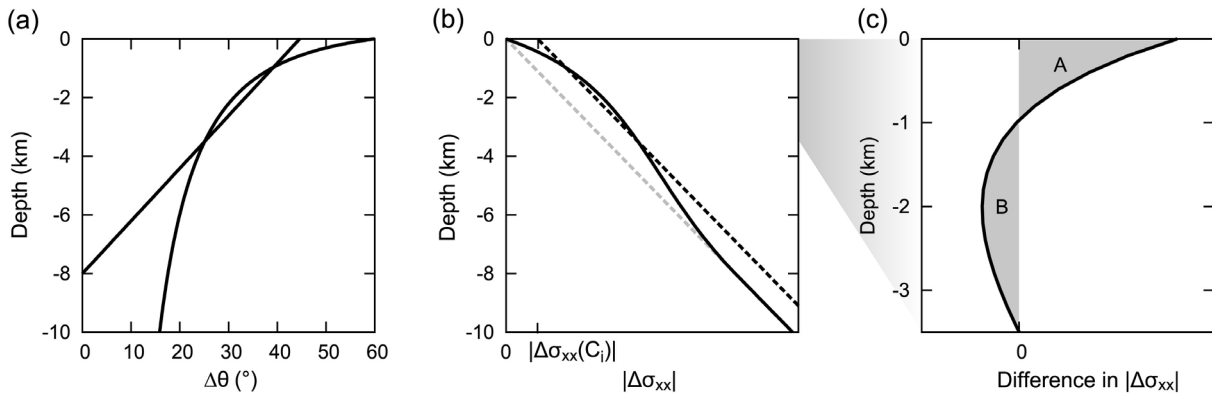


**Figure 10.** (a) A rotation envelope intersected by a curved fault profile that takes the optimal orientation below  $-8$  km and has linearly decreasing dip above that depth. (b) Differential stresses ( $\Delta\sigma_{xx}$ ) for the initial and final failure envelopes (dark and light gray dashed lines, respectively) as well as for the rotated fault (solid line), of which profile is shown in Figure 10a. (c) Variation of difference in  $\Delta\sigma_{xx}$  between the failure envelope for intact rock and the assumed fault profile, from surface to the lower intersection point. The areas of gray-shaded regions, A and B, are equal.

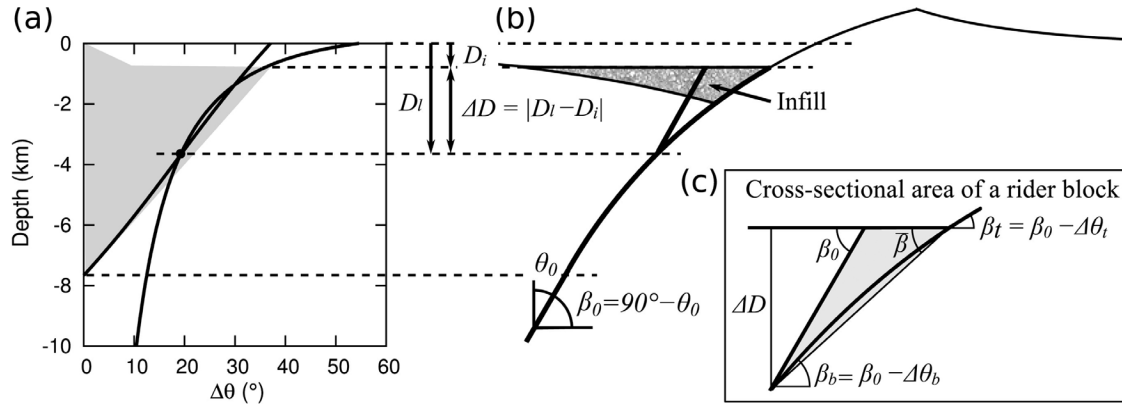


**Figure 11.** Schematic diagram explaining how the cross-sectional area of a rider block can be estimated from the  $\Delta\theta$ -depth coordinates of the lower intersection point between a fault profile and a rotation envelope.  $D_i$ : infill level;  $D_l$ : depth to the lower intersection point;  $\theta_0$ : the optimal fault orientation with respect to  $\sigma_1$ ;  $\beta_0$ : the optimal dip. See text for further details.

and friction. If there is a depth for which the force to form a splay is equal to or lower than the force to slip on the rotated fault segment then a splay fault is taken to form above that depth and create a rider block.

[28] As long as the fault rotation profile on the  $\Delta\theta$ -depth plot exceeds the rotation envelope then there is a depth range where the differential stress for breaking a new fault is less than that for continuing slip on the original faults. Such a case with a complete loss of cohesion (i.e.,  $C_f/C_i = 0$ ) on the rotated fault is illustrated in Figure 10. We assume a fault profile that deviates from the optimal orientation only above 8 km and intersects a hypothetical rotation envelope at two points as shown in Figure 10a. Differential stresses for the initial and final failure envelopes are easily calculated at each depth with equation (4) (Figure 10b, dark and light gray

dashed lines, respectively). On the shallowest part of the fault the differential stress for slip is less than that for breaking a new fault. In addition,  $|\Delta\sigma_{xx}|$  along the given fault profile (Figure 10b, solid line) is calculated using equation (4). Figure 10b shows that the difference in  $|\Delta\sigma_{xx}|$  between the initial failure envelope for intact rock and that for the given fault profile is depth-dependent, being negative over the depth range for which  $\Delta\theta$  for the fault profile exceeds the maximum allowable rotation of the fault (i.e., rotation envelope, Figure 10a) and positive otherwise. The actual variation in the difference of  $|\Delta\sigma_{xx}|$  values is plotted from the surface to the lower intersection point in Figure 10c.  $F_s(D_l)$ , the depth-integrated difference in  $|\Delta\sigma_{xx}|$  down to the depth of the lower intersection point ( $D_l$ ), should be zero for a new splay fault to cut the hanging wall from  $D_l$  to

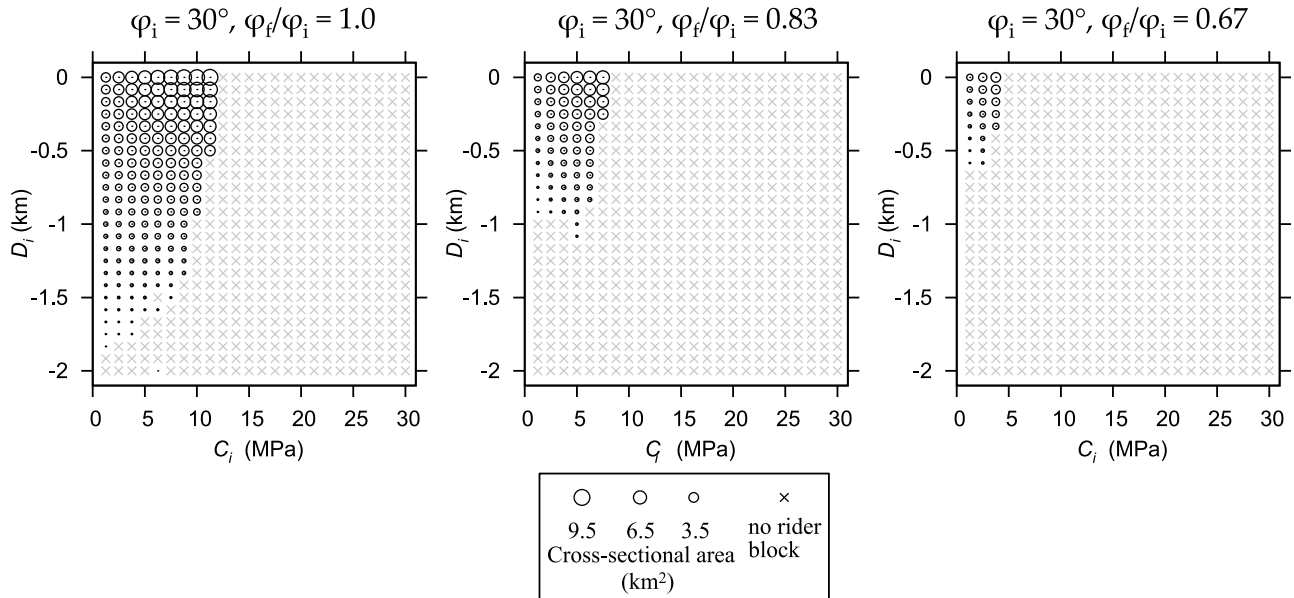


**Figure 12.** Distribution of rider block size (cross-sectional area) as a function of infill depth ( $D_i$ ), the initial cohesion ( $C_i$ ), and the ratio of reduced friction angle ( $\phi_f/\phi_i$ ). Legends show the maximum cross-sectional area for each  $\phi_f/\phi_i$  value.  $C_f$  is zero for all the cases.

surface. The fault profile shown in Figure 10a represents such a case and therefore the two gray-shaded regions in Figure 10c, regions A and B, have equal areas.

[29] The size of block, represented by cross-sectional area, can be simply computed. As a generic example, we show one fault profile domain for an infill level ( $D_i$ ) of  $-1$  km in Figure 11a. The fault profile domain is marked by gray shading. The solid straight line in the  $\Delta\theta$ –depth plot corresponds to a fault profile that has the optimal orientation below  $\sim -7.5$  km but takes an accurate shape at shallower depths. The black dot at  $\sim 3.5$  km depth shows the lower intersection point through which the fault profile intersects the rotation envelope satisfying the force-triggering condition. This fault profile can be shown in the physical space with the same depth scale as the  $\Delta\theta$ –depth plot (Figure 11b). The depth coordinate of the lower intersection point is denoted as  $D_l$ . Figure 11c shows that once  $\Delta D = |D_l - D_i|$  is determined, the size of a rider block can be approximated by the gray-shaded triangular area, which is computed as follows:

$$\text{Cross-sectional area of a rider block} = \frac{1}{2} \Delta D^2 \left( \frac{1}{\tan \bar{\beta}} - \frac{1}{\tan \beta_0} \right) \quad (7)$$

where  $\bar{\beta} = (\beta_t + \beta_b)/2$ ;  $\beta_o$ ,  $\beta_t$ , and  $\beta_b$  are the optimal dip, dips at the top and bottom of the rider block, respectively.

[30] We construct maps showing the distribution of rider block sizes for cases where the active fault is taken to have lost all cohesion (i.e.,  $C_f = 0$ ): infill level ( $D_i$ ) and initial cohesion ( $C_i$ ). Different values of the infill level ( $D_i$ ) and the initial cohesion ( $C_i$ ) are considered for three values of the ratio of friction angles ( $\phi_f/\phi_i$ ) (1.0, 0.83, and 0.67) are constructed and shown in Figure 12. Fixed in all the maps are  $C_f/C_i = 0.0$ ,  $\phi_i = 30^\circ$  and  $\rho = 1800 \text{ kg/m}^3$ . The stability field for rider blocks shrinks and the block sizes decrease as  $\phi_f/\phi_i$  decreases. For instance, the maximum size is about  $9.5 \text{ km}^2$  for  $\phi_f/\phi_i = 1.0$  but only  $3.5 \text{ km}^2$  for  $\phi_f/\phi_i = 0.67$ . The block size growth with increasing  $C_i$  is terminated abruptly because the fault profile domains are limited. As infill level increases, rider blocks become bigger and form for a wider range of  $C_i$ .

## 7. Discussion and Summary

[31] The conditions for rider block formation associated with a large-offset normal fault in an extending Mohr-Coulomb layer were quantified. A major simplifying assumption is that the minimum principle stress was taken to be horizontal everywhere and remain so during fault rotation. This may not be a bad assumption when sedimentary or volcanic material fills in the basin above an evolving normal fault. Numerical models support the assumption that the active normal fault has such a curved geometry that dip angle varies linearly with depth, and that the linearity is maintained as the fault rotates with increasing offset. Rider blocks are conjectured to form when the force to form a splay fault is less than or equal to the force to continue slip of the curved fault. The depth at which the splay diverges from the original fault is the greatest depth for which the stress difference to form an optimally oriented fault is less than that for continued slip on the rotated fault.

[32] The analytic model results depend on three variables: the reduction in cohesion on the active fault, the reduction of friction angle on the active faults, and the level of infill of the basin formed over the active fault. Consistent with predictions of *Reston and Ranero* [2011] increased infill of the fault basin promotes formation of rider blocks and large magnitude fault weakening prevents their formation. However, we show that moderate reduction in fault cohesion is necessary to make rider blocks and that friction reduction alone cannot produce blocks. The range of sizes predicted by the model is consistent with the range of observed rider blocks. Our model suggests that any process that significantly reduces fault friction, such as serpentinization of ultramafic fault rocks, can prevent rider block formation.

[33] This trend is consistent with the suggestion made by *Reston and Ranero* [2011] that rider block formation at oceanic detachment faults is facilitated by volcanic infill. The cross-sectional areas of rider blocks at well-known metamorphic and oceanic core complexes [*Davis*, 1980; *Rehrig and Reynolds*, 1980; *Reston and Ranero*, 2011] are roughly in the range of  $2\text{--}10 \text{ km}^2$ . This range of block sizes is reproduced only when friction angle is not reduced, which suggests that friction angle reduction is an unfavorable weakening mechanism for rider block formation.

[34] We note that conditions for rider block formation are antipodal to those for large-offset normal faults. According to *Lavier et al.* [2000], large-offset normal faults are favored over other modes of deformation when the amount of weakening (cohesion reduction) is large, the rate of weakening is moderate, and the brittle layer is thin. We showed in this study that rider blocks form when the amount of weakening is not too large although we have not yet considered the rate of fault weakening with offset on rider block formation. As for the thickness of brittle layer, we expect that a thicker layer would create rider blocks more easily, considering that rotation envelopes are independent of layer thickness while fault profiles for a thicker layer would pivot around a greater depth. These contrasting conditions are consistent with our proposition that observations on rider blocks (i.e., presence and geometry) can provide tight constraints on fault strength.

[35] Future work will focus on long-term numerical models for fault formation in extending brittle layer with infill of the fault basin. The idea is to simulate the development of multiple rider blocks such as are observed. We also plan to consider the effects of rate of weakening as well as erosion of rider blocks to look at data from continental core complexes. Since different fault rocks are found at different depths [e.g., *Davis et al.*, 1986; *Sibson*, 1977], the assumption of uniform material properties may have to be relaxed.

## Appendix A: Closed-Form Solutions for Allowable Rotation

### A1. General Solution to Simultaneous Reduction of Cohesion and Friction Angle

[36] We assume that cohesion is reduced to  $C_f$  from  $C_i$  and friction angle to  $\phi_f$  from  $\phi_i$  (Figure A1). From similarity between triangles (Figure A1),

$$2\Delta\theta - \Delta\theta' = \phi_i - \phi_f. \quad (\text{A1})$$

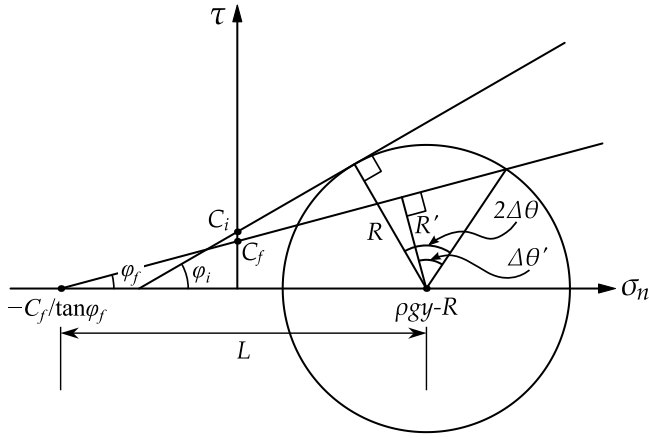


**Figure A1.** Geometry of a Mohr circle and the initial and final failure envelopes.

The difference between the center of Mohr circle and the  $x$  intercept of the reduced failure envelope is denoted as  $L$  and given by

$$L = (\rho gy - R) + C_f / \tan \phi_f, \quad (A2)$$

where  $R$  is  $\Delta \sigma_{xx}^I / 2$ :

$$R = 0.5 \Delta \sigma_{xx}^I = \frac{f_i \rho gy + C_i}{\sqrt{1 + f_i^2 + f_i}}. \quad (A3)$$

The perpendicular distance from the center of Mohr circle to the reduced envelope is denoted as  $R'$  and is equal to  $L \sin \phi_f$  (Figure A1).  $\Delta \theta'$  is then related to  $R$  and  $R'$  as follows:

$$\cos \Delta \theta' = \frac{R'}{R} = \frac{L \sin \phi_f}{R_i}. \quad (A4)$$

From (A1), (A2) and (A4), we get

$$\begin{aligned} \Delta \theta(C_i, \phi_i, C_f, \phi_f, y) \\ = 0.5 \left[ (\phi_i - \phi_f) + \cos^{-1} \left( \frac{((\rho gy - R) + \frac{C_f}{\tan \phi_f}) \sin \phi_f}{R} \right) \right]. \end{aligned} \quad (A5)$$

Note that equation (A5) is implicitly dependent on the initial cohesion ( $C_0$ ) and friction angle ( $\phi_0$ ) through the definition of  $R$ , equation (A3).

## A2. Special Case I: Cohesion Reduction Only

[37] This case has been addressed by Nur *et al.* [1986]. For completeness, their original solution is rewritten in our notation:

$$\Delta \theta(C_i, \phi_i, C_f, y) = 0.5 \cos^{-1} \left( 1 - \frac{C_i - C_f}{R} \cos \phi_i \right). \quad (A6)$$

Since  $\phi_f$  is equal to  $\phi_i$ , (equation A5) takes the form

$$\Delta \theta(C_i, \phi_i, C_f, y) = 0.5 \cos^{-1} \left( \frac{((\rho gy - R) + \frac{C_f}{\tan \phi_i}) \sin \phi_i}{R} \right). \quad (A7)$$

The equivalence of (A6) and (A7) is evident from the following relations:

$$\begin{aligned} \left( (\rho gy - R) + \frac{C_f}{\tan \phi_i} \right) \sin \phi_i &= \left( (\rho gy - R) + \frac{C_i}{\tan \phi_i} \right) \\ &\cdot \sin \phi_i - (C_i - C_f) \cos \phi_i \\ &= R - (C_i - C_f) \cos \phi_i. \end{aligned}$$

## A3. Special Case II: Friction Angle Reduction Only

[38] Since  $C_f = C_i$ , (A5) simply becomes

$$\begin{aligned} \Delta \theta(C_i, \phi_i, \phi_f, y) \\ = 0.5 \left[ (\phi_i - \phi_f) + \cos^{-1} \left( \frac{((\rho gy - R) + \frac{C_i}{\tan \phi_f}) \sin \phi_f}{R} \right) \right]. \end{aligned} \quad (A8)$$

## Appendix B: Geometry of Faults That Are Straight Lines in $\Delta \theta$ -Depth Space

[39] Let  $x = f(z)$  be a function representing a fault geometry, where  $x$  and  $z$  are horizontal and vertical (positive upward) coordinates, respectively. If the fault appears as a straight line in  $\Delta \theta$ -depth space,

$$\begin{aligned} f'(z) = \frac{dx}{dz} &= \tan \left( \frac{\pi}{2} - \beta_0 + \Delta \theta_{\max} \frac{z - z_b}{z_t - z_b} \right) \\ &= \cot \left( \beta_0 - \Delta \theta_{\max} \frac{z - z_b}{z_t - z_b} \right), \end{aligned} \quad (B1)$$

where  $\beta_0$  is the optimal dip,  $\Delta \theta_{\max}$  is the total change in dip with depth,  $z_b$  and  $z_t$  are vertical coordinates for the bottom and top of the fault, respectively. Note that the fault geometry is given as a function of vertical coordinate while

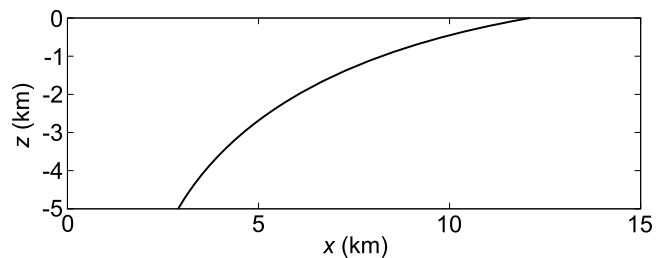


**Figure B1.** Geometry of a fault of which dip angle linearly changes from 60° to 10° with decreasing depth.

dip is defined in the usual sense, i.e., as the angle from the horizontal axis. Integration leads to

$$x = -\frac{z_t - z_b}{\Delta\theta_{\max}} \ln \left| \sin \left( \beta_0 - \Delta\theta_{\max} \frac{z - z_b}{z_t - z_b} \right) \right| + C, \quad (\text{B2})$$

where  $C$  is an integration constant. One can easily invert the above equation to express  $z$  as a function of  $x$ :

$$\frac{z - z_b}{z_t - z_b} = \frac{1}{\Delta\theta_{\max}} \left[ \beta_0 - \sin^{-1} \left( \exp \left( -(x - C) \frac{\Delta\theta_{\max}}{z_t - z_b} \right) \right) \right]. \quad (\text{B3})$$

For instance, a fault geometry is shown in Figure B1 when  $\beta_0 = 60^\circ$ ,  $\Delta\theta_{\max} = 50^\circ$ ,  $z_b = -5$  km and  $z_t = 0$ . The integration constant is determined by an additional condition like the one that the fault is centered laterally.

[40] **Acknowledgments.** We deeply thank Robert Scott for the exceptionally detailed and helpful review and an anonymous reviewer for considerate comments. This research was supported by the National Science Foundation through grant EAR-0911565 and in part through TeraGrid resources provided by Texas Advanced Computing Center under grant TG-EAR100019.

## References

- Anderson, E. M. (1942), *The Dynamics of Faulting*, 1st ed., Oliver and Boyd, Edinburgh, U. K.
- Axen, G. J. (1992), Pore pressure, stress increase, and fault weakening in low-angle normal faulting, *J. Geophys. Res.*, **97**(B6), 8979–8991, doi:10.1029/92JB00517.
- Axen, G. J. (2004), Mechanics of low-angle normal faults, in *Rheology and Deformation of the Lithosphere at Continental Margins*, edited by G. D. Karner et al., pp. 46–91, Columbia Univ. Press, New York.
- Bialas, R. W., and W. R. Buck (2009), How sediment promotes narrow rifting: Application to the Gulf of California, *Tectonics*, **28**, TC4014, doi:10.1029/2008TC002394.
- Block, L., and L. H. Royden (1990), Core complex geometries and regional scale flow in the lower crust, *Tectonics*, **9**(4), 557–567, doi:10.1029/TC009i004p00557.
- Brace, W. F., and D. L. Kohlstedt (1980), Limits on lithospheric stress imposed by laboratory experiments, *J. Geophys. Res.*, **85**(B11), 6248–6252, doi:10.1029/JB085iB11p06248.
- Buck, W. R. (1988), Flexural rotation of normal faults, *Tectonics*, **7**(5), 959–973, doi:10.1029/TC007i005p00959.
- Buck, W. R. (1991), Modes of continental lithospheric extension, *J. Geophys. Res.*, **96**(B12), 20,161–20,178, doi:10.1029/91JB01485.
- Byerlee, J. (1978), Friction of rocks, *Pure Appl. Geophys.*, **116**(4–5), 615–626, doi:10.1007/BF00876528.
- Canales, J., B. Tucholke, and J. Collins (2004), Seismic reflection imaging of an oceanic detachment fault: Atlantis megamullion (Mid-Atlantic Ridge, 30°10'N), *Earth Planet. Sci. Lett.*, **222**(2), 543–560, doi:10.1016/j.epsl.2004.02.023.
- Cann, J. R., D. K. Blackman, D. K. Smith, E. McAllister, B. Janssen, S. Mello, E. Avgerinos, A. R. Pascoe, and J. Escartin (1997), Corrugated slip surfaces formed at ridge-transform intersections on the Mid-Atlantic Ridge, *Nature*, **385**, 329–332, doi:10.1038/385329a0.
- Choi, E., L. Lavier, and M. Gurnis (2008), Thermomechanics of mid-ocean ridge segmentation, *Phys. Earth Planet. Inter.*, **171**(1–4), 374–386, doi:10.1016/j.pepi.2008.08.010.
- Coney, P. J. (1980), Cordilleran metamorphic core complexes, in *Cordilleran Metamorphic Core Complexes*, edited by M. D. Crittenden, P. J. Coney, and G. H. Davis, *Mem. Geol. Soc. Am.*, **153**, 7–34.
- Davis, G. A. (1980), Problems of intraplate extensional tectonics, western United States, in *Continental Tectonics*, pp. 84–95, Natl. Acad. of Sci., Washington, D. C.
- Davis, G., and G. Lister (1988), Detachment faulting in continental extension: Perspectives from the southwestern U.S. Cordillera, in *Processes in Continental Lithospheric Deformation*, edited by P. Sydney et al., *Spec. Pap. Geol. Soc. Am.*, **218**, 133–159.
- Davis, G. A. (1988), Rapid upward transport of mid-crustal mylonitic gneisses in the footwall of a Miocene detachment fault, Whipple Mountains, southeastern California, *Geol. Rundsch.*, **77**, 191–209, doi:10.1007/BF01848684.
- Davis, G. A., G. S. Lister, and S. J. Reynolds (1983), Interpretation of Cordilleran core complexes as evolving crustal shear zones in an extending orogen, *Geol. Soc. Am. Abstr. Programs*, **15**, 311.
- Davis, G. A., G. S. Lister, and S. J. Reynolds (1986), Structural evolution of the Whipple and South mountains shear zones, southwestern United States, *Geology*, **14**(1), 7–10, doi:10.1130/0091-7613(1986)14<7:SEOTWA>2.0.CO;2.
- Ellis, S. M., T. A. Little, L. M. Wallace, B. R. Hacker, and S. J. Buiter (2011), Feedback between rifting and diapirism can exhumate ultrahigh-pressure rocks, *Earth Planet. Sci. Lett.*, **311**, 427–438, doi:10.1016/j.epsl.2011.09.031.
- Escartin, J., G. Hirth, and B. Evans (1997), Effects of serpentinization on the lithospheric strength and the style of normal faulting at slow-spreading ridges, *Earth Planet. Sci. Lett.*, **151**(3–4), 181–189, doi:10.1016/S0012-821X(97)81847-X.
- Gans, P. B., E. L. Miller, J. McCarthy, and M. L. Ouldccott (1985), Tertiary extensional faulting and evolving ductile-brittle transition zones in the northern Snake Range and vicinity: New insights from seismic data, *Geology*, **13**(3), 189–193, doi:10.1130/0091-7613(1985)13<189:TEFAED>2.0.CO;2.
- Hubbert, M. K., and W. W. Rubey (1959), Role of fluid pressure in mechanics of overthrust faulting: I. Mechanics of fluid-filled porous solids and its application to overthrust faulting, *Geol. Soc. Am. Bull.*, **70**(2), 115–166, doi:10.1130/0016-7606(1959)70[115:ROFPI]2.0.CO;2.
- Jackson, J. A. (1987), Active normal faulting and crustal extension, in *Continental Extensional Tectonics*, edited by M. P. Coward, J. F. Dewey, and P. L. Hancock, *Geol. Soc. Spec. Publ.*, **28**, 3–17.
- Kruse, S., M. K. McNutt, J. Phipps-Morgan, L. Royden, and B. P. Wernicke (1991), Lithospheric extension near Lake Mead, Nevada: A model for ductile flow in the lower crust, *J. Geophys. Res.*, **96**(B3), 4435–4456, doi:10.1029/90JB02621.
- Lachenbruch, A. H., and J. H. Sass (1992), Heat flow from Cajon Pass, fault strength, and tectonic implications, *J. Geophys. Res.*, **97**(B4), 4995–5015, doi:10.1029/91JB01506.
- Lavier, L. L., W. R. Buck, and A. N. B. Poliakov (2000), Factors controlling normal fault offset in an ideal brittle layer, *J. Geophys. Res.*, **105**(B10), 23,431–23,442, doi:10.1029/2000JB900108.
- Martinez, F., A. M. Goodliffe, and B. Taylor (2001), Metamorphic core complex formation by density inversion and lower-crust extrusion, *Nature*, **411**(6840), 930–934, doi:10.1038/35082042.
- McGarr, A., and N. C. Gay (1978), State of stress in the Earth's crust, *Annu. Rev. Earth Planet. Sci.*, **6**(1), 405–436, doi:10.1146/annurev.ea.06.050178.002201.
- Morris, A., J. S. Gee, N. Pressling, B. E. John, C. J. MacLeod, C. B. Grimes, and R. C. Searle (2009), Footwall rotation in an oceanic core complex quantified using reoriented Integrated Ocean Drilling Program core samples, *Earth Planet. Sci. Lett.*, **287**, 217–228, doi:10.1016/j.epsl.2009.08.007.
- Mount, V. S., and J. Suppe (1987), State of stress near the San Andreas fault: Implications for wrench tectonics, *Geology*, **15**(12), 1143–1146, doi:10.1130/0091-7613(1987)15<1143:SOSNTS>2.0.CO;2.
- Nur, A., H. Ron, and O. Scotti (1986), Fault mechanics and the kinematics of block rotations, *Geology*, **14**(9), 746–749, doi:10.1130/0091-7613(1986)14<746:FMATKO>2.0.CO;2.
- Poliakov, A., and W. R. Buck (1998), Mechanics of stretching elastic-plastic-viscous layers: Applications to slow-spreading mid-ocean ridges, in *Faulting and Magmatism at Mid-Ocean Ridges*, *Geophys. Monogr. Ser.*, vol. 106, edited by W. R. Buck et al., pp. 305–323, AGU, Washington, D. C., doi:10.1029/GM106p0305.
- Rehrig, W. A., and S. J. Reynolds (1980), Geologic and geochronologic reconnaissance of a northwest-trending zone of metamorphic core complexes in southern and western Arizona, in *Cordilleran Metamorphic Core Complexes*, edited by M. D. Crittenden, P. J. Coney, and G. H. Davis, *Mem. Geol. Soc. Am.*, **153**, 131–156.
- Reston, T. J., and C. R. Ranero (2011), The 3D geometry of detachment faulting at mid-ocean ridges, *Geochem. Geophys. Geosyst.*, **12**, Q0AG05, doi:10.1029/2011GC003666.
- Scholz, C. H., R. Ando, and B. E. Shaw (2010), The mechanics of first order splay faulting: The strike-slip case, *J. Struct. Geol.*, **32**(1), 118–126, doi:10.1016/j.jsg.2009.10.007.
- Schouten, H., D. K. Smith, J. R. Cann, and J. Escartin (2010), Tectonic versus magmatic extension in the presence of core complexes at slow-spreading ridges from a visualization of faulted seafloor topography, *Geology*, **38**(7), 615–618, doi:10.1130/G30803.1.



- Scott, R. J., and G. S. Lister (1992), Detachment faults: Evidence for a low-angle origin, *Geology*, 20(9), 833–836, doi:10.1130/0091-7613(1992)020<0833:DFFEFAL>2.3.CO;2.
- Sibson, R. H. (1977), Fault rocks and fault mechanisms, *J. Geol. Soc.*, 133(3), 191–213, doi:10.1144/gsjgs.133.3.0191.
- Sibson, R. H. (1985), A note on fault reactivation, *J. Struct. Geol.*, 7(6), 751–754, doi:10.1016/0191-8141(85)90150-6.
- Smith, D. K., J. Escartin, H. Schouten, and J. R. Cann (2008), Fault rotation and core complex formation: Significant processes in seafloor formation at slow-spreading mid-ocean ridges (Mid-Atlantic Ridge, 13°–15°N), *Geochem. Geophys. Geosyst.*, 9, Q03003, doi:10.1029/2007GC001699.
- Spencer, J. E. (1984), Role of tectonic denudation in warping and uplift of low-angle normal faults, *Geology*, 12(2), 95–98, doi:10.1130/0091-7613(1984)12<95:ROTDIW>2.0.CO;2.
- Townend, J., and M. D. Zoback (2000), How faulting keeps the crust strong, *Geology*, 28(5), 399–402, doi:10.1130/0091-7613(2000)28<399:HFKTCS>2.0.CO;2.
- Tucholke, B. E., J. Lin, and M. C. Kleinrock (1998), Megamullions and mullion structure defining oceanic metamorphic core complexes on the Mid-Atlantic Ridge, *J. Geophys. Res.*, 103(B5), 9857–9866, doi:10.1029/98JB00167.
- Turcotte, D. L., and G. Schubert (2002), *Geodynamics: Applications of Continuum Physics to Geological Problems*, 2nd ed., Cambridge Univ. Press, Cambridge, U. K.
- Vening-Meinesz, F. A. (1950), Les grabens Africains résultants de compression ou de tension de la croûte terrestre?, *Bull. Inst. R. Colon. Belg.*, 21, 539–552.
- Wernicke, B. (1981), Low-angle normal faults in the Basin and Range Province: Nappe tectonics in an extending orogen, *Nature*, 291, 645–648, doi:10.1038/291645a0.
- Wernicke, B., and G. J. Axen (1988), On the role of isostasy in the evolution of normal fault systems, *Geology*, 16(9), 848–851, doi:10.1130/0091-7613(1988)016<0848:OTROI>2.3.CO;2.
- Wills, S., and W. R. Buck (1997), Stress-field rotation and rooted detachment faults: A Coulomb failure analysis, *J. Geophys. Res.*, 102(B9), 20,503–20,514, doi:10.1029/97JB01512.
- Yin, A. (1989), Origin of regional, rooted low-angle normal faults: A mechanical model and its tectonic implications, *Tectonics*, 8(3), 469–482, doi:10.1029/TC008i003p00469.
- Zoback, M. D., and J. H. Healy (1992), In situ stress measurements to 3.5 km depth in the Cajon Pass scientific research borehole: Implications for the mechanics of crustal faulting, *J. Geophys. Res.*, 97(B4), 5039–5057, doi:10.1029/91JB02175.

W. R. Buck, Lamont-Doherty Earth Observatory, Earth Institute at Columbia University, PO Box 1000, 61 Rt. 9W, Palisades, NY 10964, USA.

E. Choi, Institute for Geophysics, University of Texas, J.J. Pickle Research Campus, Bldg. 196, 10100 Burnet Rd., R2200, Austin, TX 78758-4445, USA. (echoi@ig.utexas.edu)